Feasibility Study of a Multi-Tilt-rotor Aircraft as the Artemis Lunar Training Vehicle

Jing Pei*, Jared A. Grauer†, Jason R. Welstead‡, Luke J. Miller§
NASA Langley Research Center, Hampton, Virginia, 23681

Han Woong Bae¶
Marshall Space Flight Center, Huntsville, Alabama, 35851

The Lunar Landing Research Vehicles (LLRVs) and the Lunar Landing Training Vehicles (LLTVs) provided astronauts of the Apollo program with essential experience and confidence required to complete the missions, and contributed to six successful manned landings on the moon. The primary challenge in terrestrial training was being able to replicate the ratio of tilt angle to linear acceleration that a pilot would experience in lunar gravity. Presently, as the Artemis program seeks to return humans to the Moon by 2025, engineers are evaluating suitable platforms to serve as an In-Flight Trainer (IFT) or Artemis Lunar Training Vehicle (ALTV) for astronauts training in the task of manual landing. The program is investigating the viability of current technology in the field of electric vertical takeoff and landing (eVTOL) vehicles and is evaluating using a multi-tilt-rotor aircraft platform as a candidate for a preliminary ALTV. The tilt-rotor capability enables the vehicle attitude to be decoupled from its flight path, which is a crucial requirement in realistically simulating lunar gravity on Earth. Other key considerations include compensating for a lack of aerodynamic forces while flying through the atmosphere of Earth, as well as the ability to simulate the dynamics of multiple different lander designs for the Human Landing System (HLS) program. This paper details the feasibility study and presents a preliminary flight control architecture for an IFT based on a notional multi-tilt-rotor platform. The model-following control law, based on nonlinear dynamic inversion (NDI), removes the need for gain scheduling. The inner-loop dynamic control allocation strategy consists of a static portion that is optimized offline for trim while compensating for the difference in gravity and a dynamic portion that is computed in real time. The reference model consists of the full closed-loop dynamics of a generic HLS design. The modularity of the flight control architecture enables evaluation of multiple HLS concepts with minimal modifications to the control law. Simulation results of the multi-tilt-rotor configuration following the final portion of the Apollo 11 descent trajectory are shown.

Nomenclature

g	=	gravitational acceleration, m/s^2	S	=	reference area, m^2
I	=	Inertia Matrix, N-m^2	L_{ref}	=	reference length, m
m	=	aircraft mass, kg	α	=	angle-of-attack, deg
q	=	body-axis pitch rates, rad/s	γ	=	flight path angle, deg
q_∞	=	dynamic pressure, N/m^2	δ	=	rotor gimbal angle, deg

*Aerospace Engineer, Atmospheric Flight Entry Systems Branch.
†Research Engineer, Dynamic Systems and Controls Branch, MS 308, Associated Fellow AIAA.
‡Aerospace Engineer, Aeronautic Systems Branch.
§Aerospace Engineer, Flight Dynamics Branch.
¶Aerospace Engineer, Navigation Guidance & Controls Branch

θ = pitch angle, deg
T = rotor thrust, N
C_L, C_D = lift, drag force coefficient
C_Z, C_X = normal, axial force coefficient
C_m = pitching moment coefficient
ω = angular velocity, rad/s
V = velocity vector, m/s
B = control effectivenss matrix

Subscripts

des = desired
cmd = commanded
i = index for rotor

Superscripts

$^{-1}$ = matrix inverse
^{T} = transpose
$\dot{}$ = time derivative
$\tilde{}$ = increment

Acronyms

LLRV = Lunar Landing Research Vehicle
LLTV = Lunar Landing Training Vehicle
LEM = Lunar Excursion Module
UAM = Urban Air Mobility
IFT = In-Flight Trainer
ALTV = Artemis Lundar Training Vehicle
eVTOL = Electric Vertical Takeoff and Landing
HLS = Human Landing System
NDI = Nonlinear Dynamic Inversion

I. Introduction

On July 20, 1969, Neil Armstrong and Edwin (Buzz) Aldrin piloted the Apollo 11 Lunar Module, dubbed "Eagle," to a safe landing on the Sea of Tranquility. Subsequently, five more successful landings took place during the Apollo 12 and 14–17 missions under the manual control of the flight commanders. Each landing encountered different topography and was piloted manually under the supervision of the flight commander.[2] The Lunar Landing Research Vehicle (LLRV) program[1–6] was developed to provide the astronauts with sufficient training and confidence in the daunting task of landing on the Moon. Later in the program, a modified version of the LLRV, the Lunar Landing Training Vehicle (LLTV), was developed to better match the characteristics of the Lunar Excursion Module (LEM). The LLRV and LLTV proved to be indispensable in the training of the Apollo astronauts and gained high remarks from the commanders.[1,2,7]

Today, the Human Landing System (HLS), part of NASA's Artemis Program,[8] seeks to land the first woman and next man at the lunar south pole in 2025. In a risk assessment document provided by the NASA Crew Office, the final descent and landing phase is deemed the most critical and involves the greatest risk to the crew and the mission. The primary challenge in training HLS pilots is due to the gravitational difference between the Moon and the Earth. A lunar lander requires a tilt angle nearly six times as large as an Earth-bound vertical take-off and landing (VTOL) vehicle to achieve the same desired linear acceleration, $\dot{V}_{des}$, as illustrated in Fig. 1. Neil Armstrong was quoted saying in Ref. [1], "Decelerating the vehicle is like stopping a putt on a fast down hill green." Furthermore, the manual lunar landing task is a dynamic, skills-based task requiring a high level of sensorimotor coordination. No fixed-base or motion-base simulations can fully replicate the physiological cues and psychological stressors. These arguments justify the need for an HLS In-Flight Trainer (IFT) that would serve the same purpose as the Apollo LLRV/LLTV.

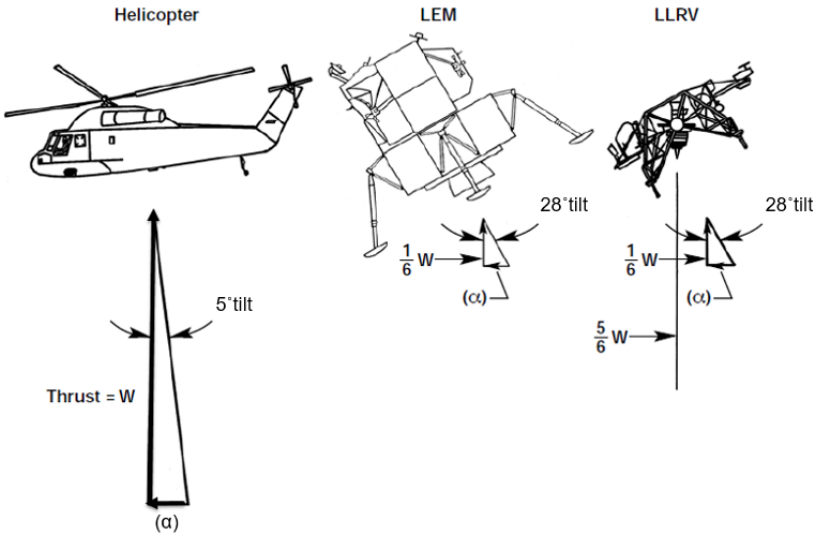

Figure 1. Bank angle comparison between earthbound VTOL vehicles with LEM and LLRV, adapted from Ref. [2].

Electric vertical take-off and landing (eVTOL) vehicles are gaining much popularity in the emerging market of urban air mobility.[9] The majority of eVTOL designs consist of rotors that are allowed to gimbal which enables the vehicle attitude to be decoupled from its flight path. This feature is essential in simulating the ratio of tilt angle to linear acceleration for a lunar IFT. Given programmatic considerations including cost, safety, maintainability, and schedule, the HLS program is pursuing a multi-tilt-rotor vehicle in the same class as the Joby S4 configuration shown in Fig. 2 for an HLS IFT.

Figure 2. Joby S4 multi-tilt-rotor aircraft (Ref. [10]).

The notional tilt-rotor configuration consists of six rotors possessing gimbaling capabilities in the pitch axis only. Therefore, simulation of lunar gravity is only possible in the longitudinal plane and not the lateral plane. This drawback was deemed acceptable by the IFT feasibility team since like Apollo,[11,12] the HLS trajectories from pitch up to final touchdown primarily involve downrange target redesignations with minimal crossrange steering. Unlike the LLRV/LLTV, which were similar in design as the actual LEM, the tilt-rotor configuration does not resemble a rocket-powered lander. The object of the flight control design is to make the aircraft behave like a variable stability vehicle such that it is capable of replicating the closed-loop dynamics and landing trajectories of multiple HLS concepts. The widely-used model-following or nonlinear dynamic inversion (NDI)[9,13–16] flight controls architecture was selected due to its intuitive nature, explicit model-following behavior, ability to easily evaluate different reference models, and the existence of linear stability margins. The control law computes the necessary rotor thrusts, gimbal angles, and control surface deflections to achieve the desired acceleration commands.

This paper summarizes the assessment performed in using a multi-tilt-rotor configuration as a potential IFT candidate from a flight controls perspective. This paper is organized as follows. Section II provides a

brief description of the generic tilt-rotor configuration used in this study and a 3 degree-of-freedom (DoF) mathematical model of the aircraft. Section III details the flight control architecture that would enable the tilt-rotor vehicle to operate in lunar simulation mode, including an optimized trim map, NDI control law, and dynamic control allocator. Section IV provides simulation results of the tilt-rotor configuration following the final two minutes of the Apollo 11 descent and landing trajectory. Section V summarizes the work.

II. Vehicle Description

A 3 DoF mathematical model of the notional tilt-rotor configuration is provided in this section. Note that since lunar simulation mode is only possible in the longitudinal axis, a 3 DoF model is deemed sufficient for the scope of this study. Notional limits for the thrust, T, which is related to power levels and max take-off weight, and gimbal angle, δ, are provided for each pair of rotors in Table 1. Definitions and nomenclatures are shown in Fig. 3. Since this is strictly a 3 DoF analysis, the principle of symmetry are applied to the rotors. The rotor numbering system is as follows: the front pair is treated as a single rotor with a subscript 1, followed by the middle pair treated as a single rotor with a subscript 3, and the aft pair treated with a subscript 5.

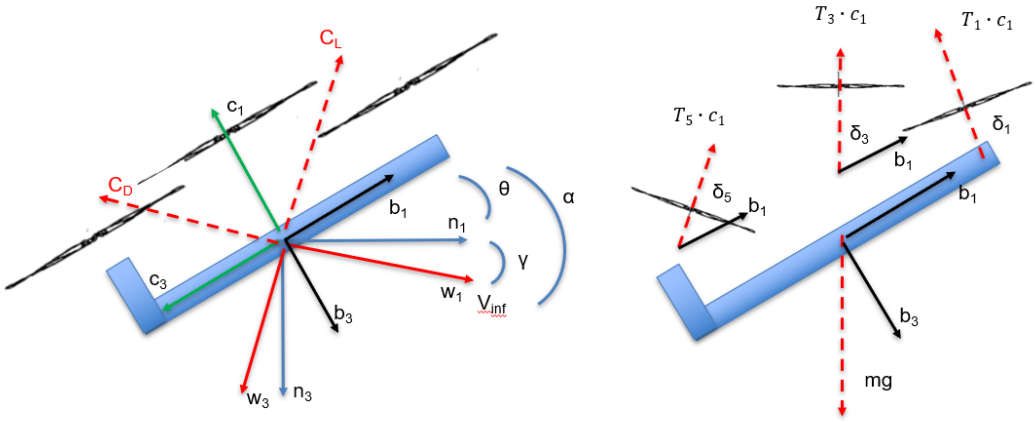

Figure 3. Vehicle coordinate system and flight variable definitions.

Table 1. Notional rotor thrust and gimbal position limits.

Parameter	Minimum	Maximum
δ_1	0 deg	95 deg
δ_3	0 deg	125 deg
δ_5	0 deg	110 deg
T_1	2023 N	6700 N
T_3	2023 N	6700 N
T_5	2023 N	6700 N

In Fig. 3, $\hat{\mathbf{n}}_1$, $\hat{\mathbf{n}}_2$, and $\hat{\mathbf{n}}_3$ constitute a set of right-handed orthogonal unit vectors fixed in a local-vertical and local-horizontal inertial frame N. Unit vector $\hat{\mathbf{n}}_3$ is vertical, and directed downward. Unit vector $\hat{\mathbf{n}}_1$ is horizontal, and directed downrange. The vectors $\hat{\mathbf{b}}_1$, $\hat{\mathbf{b}}_2$, and $\hat{\mathbf{b}}_3$ denote the vehicle body frame, with $\hat{\mathbf{b}}_1$ pointing towards the nose of the vehicle and $\hat{\mathbf{b}}_2$ in the direction of the starboard wing. The vectors $\hat{\mathbf{w}}_1$, $\hat{\mathbf{w}}_2$, and $\hat{\mathbf{w}}_3$ denote the wind frame with the drag and lift coefficients (C_D and C_L) in the $-\hat{\mathbf{w}}_1$ and $-\hat{\mathbf{w}}_3$ directions, respectively. The vectors $\hat{\mathbf{c}}_1$, $\hat{\mathbf{c}}_2$, and $\hat{\mathbf{c}}_3$ denote the gimbal frame applicable for each set of rotors. The direction of thrust for each pair of rotors is aligned with the associated $\hat{\mathbf{c}}_1$. The variables θ and γ are

the pitch and flight path angles, respectively. The angle of attack is defined as

$$\alpha = \theta + \gamma \tag{1}$$

The direction cosine matrices between the body frame and the inertial, gimbal, and wind frames are provided in Tables 2 through 4.

Table 2. Direction cosine matrix [BN].

	$\hat{\mathbf{n}}_1$	$\hat{\mathbf{n}}_2$	$\hat{\mathbf{n}}_3$
$\hat{\mathbf{b}}_1$	$\cos\theta$	0	$-\sin\theta$
$\hat{\mathbf{b}}_2$	0	1	0
$\hat{\mathbf{b}}_3$	$\sin\theta$	0	$\cos\theta$

Table 3. Direction cosine matrix [CB].

	$\hat{\mathbf{b}}_1$	$\hat{\mathbf{b}}_2$	$\hat{\mathbf{b}}_3$
$\hat{\mathbf{c}}_1$	$\cos\delta$	0	$-\sin\delta$
$\hat{\mathbf{c}}_2$	0	1	0
$\hat{\mathbf{c}}_3$	$\sin\delta$	0	$\cos\delta$

Table 4. Direction cosine matrix [BW].

	$\hat{\mathbf{w}}_1$	$\hat{\mathbf{w}}_2$	$\hat{\mathbf{w}}_3$
$\hat{\mathbf{b}}_1$	$\cos\alpha$	0	$-\sin\alpha$
$\hat{\mathbf{b}}_2$	0	1	0
$\hat{\mathbf{b}}_3$	$\sin\alpha$	0	$\cos\alpha$

The planar equations of motion, describing the longitudinal motion (2 translation and 1 rotation) along $\hat{\mathbf{b}}_3$, $\hat{\mathbf{b}}_1$, and $\hat{\mathbf{b}}_2$, are as follows:

$$m\dot{w} - qu = \Sigma\mathbf{F} \cdot \hat{\mathbf{b}}_3 = -T_5 \sin\delta_5 - T_3 \sin\delta_3 - T_1 \sin\delta_1 + mg\cos\theta + q_\infty S C_Z \tag{2}$$

$$m\dot{u} + qw = \Sigma\mathbf{F} \cdot \hat{\mathbf{b}}_1 = T_5 \cos\delta_5 + T_3 \cos\delta_3 + T_1 \cos\delta_1 - mg\sin\theta + q_\infty S C_X \tag{3}$$

$$I_{yy}\dot{q} = \Sigma\mathbf{M} \cdot \hat{\mathbf{b}}_2 = (\sum_{i=1}^{3} \mathbf{r}^{OP_{2i-1}} \times T_{2i-1}\hat{\mathbf{c}}_1) \cdot \hat{\mathbf{b}}_2 + q_\infty S L_{\text{ref}} C_m \tag{4}$$

where rotor thrust, gravitational forces, and aerodynamic effects have been substituted for the applied forces and moments on the vehicle. The terms q_∞, S, L_{ref} are the dynamic pressure, reference area, and reference length, respectively. The term r^{OP} is the position vector from the vehicle center of mass to the rotor force application point.

Notional aerodynamics coefficients C_L, C_D, and C_m are shown in Fig. 4 with respect to α for the rotorless vehicle configuration. The 0 to 44 deg range was generated using VSPAERO[17] assuming linearity in the low-α region while the nonlinear lift regions were constructed using flat-plate theory.

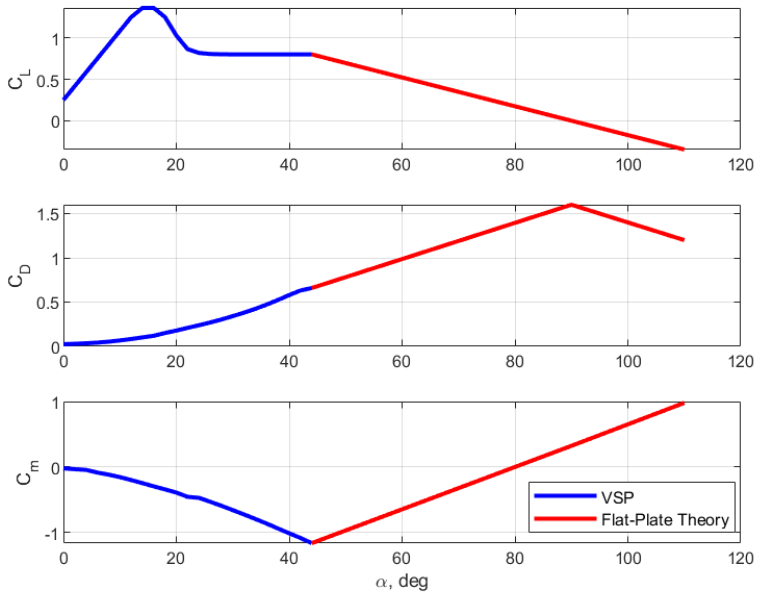

Figure 4. Notional 3 DoF Aerodynamic Model.

III. Flight Control Design

A. Overview

As discussed in Sec. I, the primary feature of the IFT is being able to compensate for the difference in gravity between the Moon and the Earth. In order to match the ratio of the tilt angle to linear acceleration of the LEM, the LLRV used a center-mounted gimbaled jet engine to compensate for 5/6 g. During lunar simulation mode, the engine would remain vertical with respect to the Earth regardless of the vehicle attitude (local-vertical mode). The remaining 1/6 g was supported by a pair of lifting rockets that were fixed with the vehicle body frame. On/Off attitude rockets were used to control the vehicle attitude which, in combination with the thrust of the lifting rockets, imparted translational motion.[4,6]

The initial concept for the Artemis IFT control architecture during this feasibility study was to replicate the LLRV/LLTV strategy by using the middle pair of rotors, which are closest to the vehicle center of mass along the vehicle $\hat{\mathbf{b}}_1$ axis, to carry the 5/6 g while the rest of the rotors provided the remaining 1/6 g as well as attitude control about the pitch axis. This concept was deemed infeasible due to the blades stalling as a result of high disk loading. In addition, the power required exceeded the maximum instantaneous power limit. Since the ultimate objective is to match the ratio of tilt angle to linear acceleration as a lander would experience on the Moon, the alternative solution pursued here is to solve for a set of rotor thrusts and gimbal angles such that the desired ratio can be achieved while trimming the vehicle, subject to hardware constraints such as gimbal position limits. Detailed formulation of this constrained optimization problem is discussed in the following subsection. This trim map can be computed offline and stored as a look-up table.

The high-level block diagram of the nonlinear dynamic inversion based architecture is illustrated in Fig. 5. The inputs are pilot commands via stick inputs. The reference model block captures the closed-loop dynamics of the HLS lander designs with the command mode being Rate Command Attitude Hold RCAH or Attitude Command Velocity Hold (ACVH) for maneuvering downrange and ROD (Rate of Descent) for altitude control. The outputs of the reference model block are the desired linear and angular velocities/accelerations (V_{ref}, $\dot{V}_{\text{ref}}$, ω_{ref}, $\dot{\omega}_{\text{ref}}$). The core of the control law is the NDI block which takes in linear and angular acceleration commands and "inverts" the aircraft dynamics, including aerodynamics and gyroscopic effects. Hence, an onboard model of the aircraft is required. The control allocator computes the necessary rotor thrusts, gimbal angles, and control surface deflections to enable the tilt-rotor aircraft to achieve the desired dynamics. Since the onboard model will never perfectly match the actual aircraft, a proportional-plus-integral

(PI) compensator is in place to reduce the error between the desired dynamics and the actual dynamics due to modeling errors, such as uncertainties in the aerodynamic tables[13] and other unmodeled dynamics.

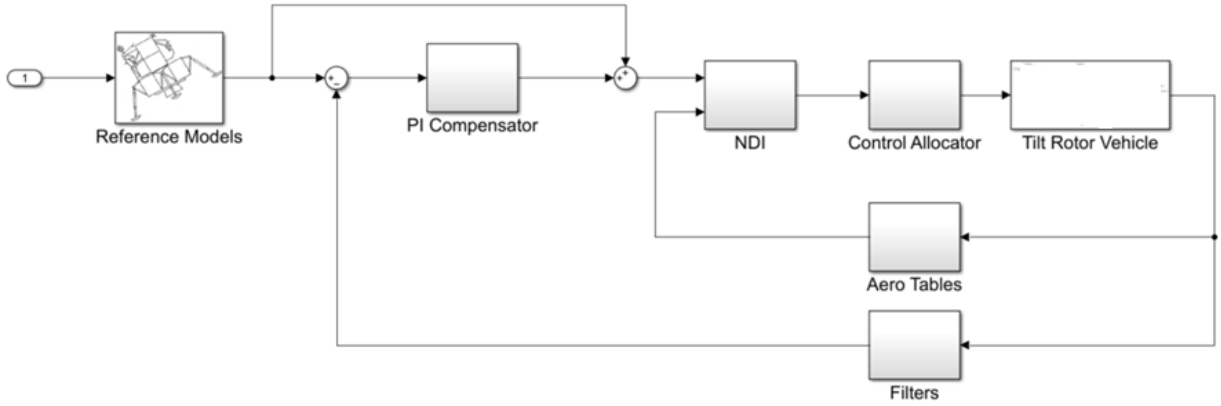

Figure 5. Top-level flight control architecture.

B. Trim Map

The purpose of the trim map is to match the ratio of tilt angle to linear acceleration as a lander would experience on the Moon while ensuring thrust equals weight and zero pitching moment at a given static pitch angle. Starting from Eqs. (2) to (4), ignoring aerodynamics, and rewriting the translation equations of motion in the inertial frame, Eqs. (5) and (6) below satisfy the thrust = weight constraint along $\hat{\mathbf{n}}_3$ and trimming the moments along $\hat{\mathbf{b}}_2$, where $\dot{V}_z$ represents acceleration along $\hat{\mathbf{n}}_3$. Equation (7) matches the desired linear acceleration, $\dot{V}_{x,des}$ for a given θ along $\hat{\mathbf{n}}_1$. The variables X and Z represents the locations of the rotors with respect to the vehicle center of mass along $\hat{\mathbf{b}}_1$ and $\hat{\mathbf{b}}_3$.

$$0 = m\dot{V}_z = -\sum_{i=1}^{3} T_{2i-1} \sin(\theta + \delta_{2i-1}) + mg \tag{5}$$

$$0 = I_{yy}\dot{q} = \sum_{i=1}^{3} T_{2i-1}(X_{2i-1} \sin\delta_{2i-1} + Z_{2i-1} \cos\delta_{2i-1}) \tag{6}$$

$$m\dot{V}_{x,des} = -\frac{1}{6} mg \tan\theta = \sum_{i=1}^{3} T_{2i-1} \cos(\theta + \delta_{2i-1}) \tag{7}$$

Equations (5) to (7) can be formulated as a constrained optimization problem and solved with the `fmincon.m` function[19] in MATLAB®. The cost function, F, is the minimization of the Euclidean norm of the rotor thrusts and gimbal angles away from nominal values of T_o and δ_o. In order to retain maximum amout of control authority, the middle value in the thrust and gimbal limits shown in Table 1 were selected for T_o and u_o respectively. W_T and W_δ are the weights on thrust and gimbal in the cost function. The variables lb and ub are the thrust and gimbal lower and upper limits specified in Table 1.

$$
\begin{aligned}
\min \quad & F = W_T||T - T_o||^2 + W_\delta||\delta - \delta_o||^2 \\
\text{s.t.} \quad & 0 = m\dot{V}_z = -\sum_{i=1}^{3} T_{2i-1}\sin(\theta + \delta_i) + mg \\
& 0 = I_{yy}\dot{q} = \sum_{i=1}^{3} T_{2i-1}(X_{2i-1}\sin\delta_{2i-1} + Z_{2i-1}\cos\delta_{2i-1}) \\
& \dot{V}_{x,des} = -\frac{1}{6}mg\tan\theta = \sum_{i=1}^{3} T_{2i-1}\cos(\theta + \delta_{2i-1}) \\
& lb \le x \le ub \quad x = [T_1 ... T_5 \quad \delta_1 ... \delta_5]^T
\end{aligned}
\tag{8}
$$

Figure 6 illustrates the trim map for θ ranging from -20 to 75 deg. Each blue circles represents the trim solution at a given θ. The red dashed lines represent the thrust and gimbal actuation limits for rotor pairs 1, 3, and 5. In the event θ exceeds the specified range, one or more constraint(s) would be violated. This constrains the vehicle pitch attitude to be within -20 to 75 deg during lunar simulation mode. If θ exceeds 75 deg, $T_{1,2}$ would violate the upper thrust limit of 6700 N. On the other hand, if θ drops below -20 deg, $\delta_{3,4}$ would violate the max gimbal limit of 125 deg. All Lunar landing trajectories consist of a pitch-over event as the vehicle approaches the landing site with reduced foward velocity and θ close to zero (near-vertical). Prior to the event, the pitch angles are large as the main engine nulls out much of the downrange velocity, the 75 deg operational limit would place an upper bound on portions of the descent trajectory the IFT can replicate. Note that propeller-wing interference effects on the performance of the props are not considered here. Reference [20] describes significant interference effects need to be factored into the trim solutions as the design matures.

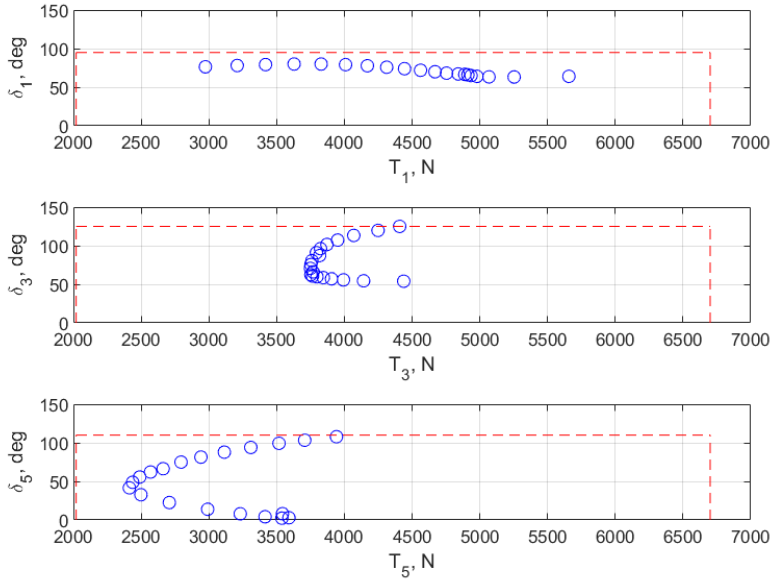

Figure 6. Trim map for lunar simulation with constraints.

C. Reference Model

The primary benefit of selecting the NDI architecture is the ease with which the tilt-rotor aircraft can be augmented into a variable stability aircraft by switching out the reference model. The reference model shown in Fig. 5 represents the HLS dynamics which the IFT is expected to follow. The reference model will vary in complexity depending on the level of fidelity of HLS dynamics is to be emulated. It can be as simple as

a second-order transfer function model[13] or as complicated as the closed-loop model accounting for effects such as delays, structural, slosh, and actuator dynamics, etc. Figure 7 is a notional illustration of an HLS reference model. Inputs to the reference model are pilot inputs such as commands via the rotational or translational hand controllers (RHC/THC). The outputs of the reference model block are the linear and angular velocities/accelerations (V_{ref}, $\dot{V}_{\text{ref}}$, ω_{ref}, $\dot{\omega}_{\text{ref}}$) the IFT is expected to follow. The manual control mode could be RCAH using the RHC and ROD using a toggle like the Apollo P66 mode.[11]

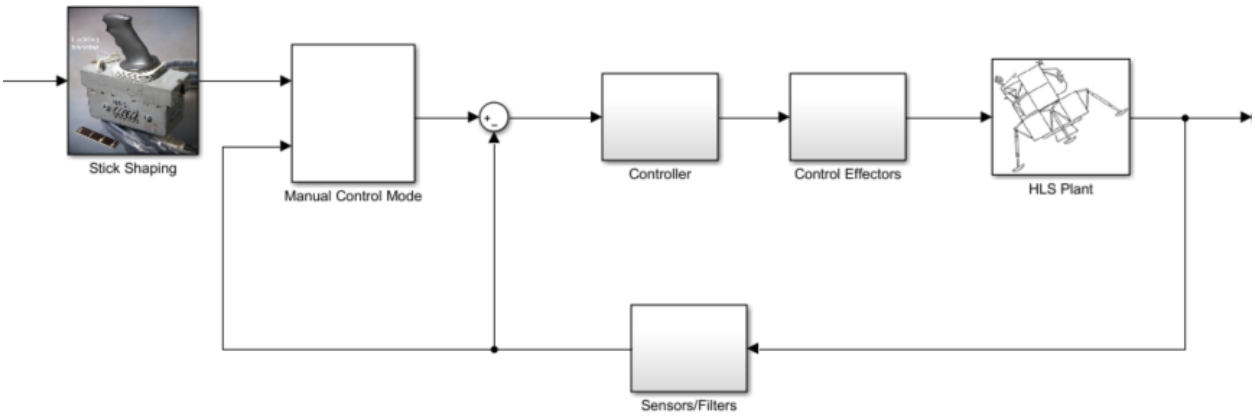

Figure 7. HLS reference model example.

D. Nonlinear Dynamic Inversion

The nonlinear dynamic inversion technique is based on the concept of conservation of linear and angular momentum.[13] Reference [14] refers to the inner loop as the feedback linearization loop. The goal of the inner loop is to make the aircraft behave like a double integrator by "canceling out" system dynamics such as gyroscopics, aerodynamics, etc. The outer, or tracking loop, provides robustness to the design to compensate for uncertainties in the model of the aircraft used for the feedback linearization. A PI compensator[13] has been shown to work well in Ref. [13] and hence was adopted in this work. A large value of outer loop gain margin correlates to ensuring errors in the aerodynamic modeling or control effector effectiveness will not drive the system unstable. Equations (9) and (10) are the generic NDI equations accounting for gravity and aerodynamics. $\dot{\mathbf{V}}_{\text{cmd}}$ and $\dot{\omega}_{\text{cmd}}$ are the commanded (desired) linear and angular accelerations.

$$\mathbf{F}_{\text{req}} = m\dot{\mathbf{V}}_{\text{cmd}} + \boldsymbol{\omega} \times m\mathbf{V} - \mathbf{F}_{\text{aero}} - \mathbf{F}_{\text{grav}} \tag{9}$$

$$\mathbf{M}_{\text{req}} = I\dot{\omega}_{\text{cmd}} + \boldsymbol{\omega} \times I\boldsymbol{\omega} - \mathbf{M}_{\text{aero}} \tag{10}$$

Equations (11) to (13) are the simplified 3 DoF NDI equations with the translational components expressed in $\hat{\mathbf{n}}$. Note that the gyroscopic terms vanish in these equations due to the planar assumption. $\dot{q}_{\text{cmd}}$, $\dot{V}_{z,\text{cmd}}$, and $\dot{V}_{x,\text{cmd}}$ are the commanded pitch and linear accelerations which consist of signals from the reference model directly (discussed in Subsec. C), and the output of the PI compensator, which corrects for errors between the reference model and the IFT. $\mathbf{F}_{\text{req}} \cdot \hat{\mathbf{n}}_3, \mathbf{F}_{\text{req}} \cdot \hat{\mathbf{n}}_1, \mathbf{M}_{\text{req}} \cdot \hat{\mathbf{b}}_2$ are the required forces and moment from the IFT to achieve the commands while "canceling out" effects of gravity and aerodynamics. Figure 8 is an illustration of the pitch channel Nichols and Bode diagrams used to assess the stability margins.

$$\mathbf{F}_{\text{req}} \cdot \hat{\mathbf{n}}_3 = m\dot{V}_{z,\text{cmd}} + mg - q_\infty S C_L \hat{\mathbf{w}}_3 \cdot \hat{\mathbf{n}}_3 - q_\infty S C_D \hat{\mathbf{w}}_1 \cdot \hat{\mathbf{n}}_3 \tag{11}$$

$$\mathbf{F}_{\text{req}} \cdot \hat{\mathbf{n}}_1 = m\dot{V}_{x,\text{cmd}} - q_\infty S C_L \hat{\mathbf{w}}_3 \cdot \hat{\mathbf{n}}_1 - q_\infty S C_D \hat{\mathbf{w}}_1 \cdot \hat{\mathbf{n}}_1 \tag{12}$$

$$\mathbf{M}_{\text{req}} \cdot \hat{\mathbf{b}}_2 = I_{\text{yy}}\dot{q}_{\text{cmd}} + q_\infty S L_{\text{ref}} C_m \tag{13}$$

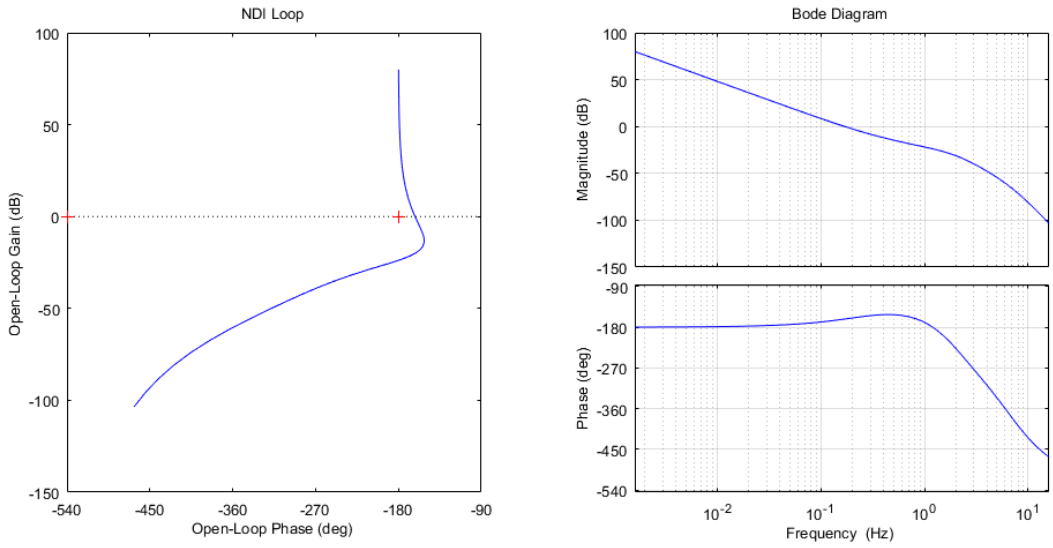

Figure 8. Pitch channel Nichols and Bode Diagrams.

E. Control Allocation

The objective of the control allocator or mixer is to map the output of the NDI ($\mathbf{F}_{\text{req}}$, $\mathbf{M}_{\text{req}}$) into thrust/gimbal commands to the six rotors and control surfaces. The HLS approach and landing trajectories may require the IFT to operate at large angles-of-attack, thus reducing the effectiveness of the tilt-rotor aerodynamic control surfaces. As a result, the control surfaces were ignored for the scope of this study. The control allocation solution consists of two parts as shown in Eqs. (14) and (15):

a) a static/baseline portion which involves the trim solution as a function of θ as discussed in Subsec. B, denoted by $\mathbf{M}_o$ and $\mathbf{F}_o$

b) a dynamic/incremental portion that computes a local control effectiveness matrix by linearizing about the operating θ, denoted by $\Delta\mathbf{M}$ and $\Delta\mathbf{F}$. u_o represents the trimmed thrust and gimbal angles and $\tilde{u}$ indicates deviations about those trimmed values shown in Eqs. (16) and (17)

$$\mathbf{M}_{\text{req}} = \mathbf{M}_o(\theta, u_o) + \Delta\mathbf{M}(u_o, \tilde{u}) \tag{14}$$

$$\mathbf{F}_{\text{req}} = \mathbf{F}_o(\theta, u_o) + \Delta\mathbf{F}(\theta, u_o, \tilde{u}) \tag{15}$$

$$u_o = [T_{1o} \dots T_{5o} \quad \delta_{1o} \dots \delta_{5o}]^T \tag{16}$$

$$\tilde{u} = [\tilde{T_1} \dots \tilde{T_5} \quad \tilde{\delta_1} \dots \tilde{\delta_5}]^T \tag{17}$$

Starting from Eqs. (5) to (7), one can take the partials of $\mathbf{M}$ and $\mathbf{F}$ with respect to $\tilde{u}$ to obtain analytical expressions for the rows of the B matrix shown in Eqs. (18) to (20). For implementation purposes, the B matrix can be computed onboard the aircraft in real-time as the operating θ varies. For the present 3 DoF vehicle model, the B matrix is a size of 3×6.

$$\frac{\delta\mathbf{F} \cdot \hat{\mathbf{n}}_3}{\delta\tilde{u}} = -[\sin(\theta_o + \delta_{1o}) \dots \sin(\theta_o + \delta_{5o}) \quad T_{1o}\cos(\theta_o + \delta_{1o}) \dots T_{5o}\cos(\theta_o + \delta_{5o})] \tag{18}$$

$$\frac{\delta\mathbf{F} \cdot \hat{\mathbf{n}}_1}{\delta\tilde{u}} = [\cos(\theta_o + \delta_{1o}) \dots \cos(\theta_o + \delta_{5o}) \quad -T_{1o}\sin(\theta_o + \delta_{1o}) \cdots -T_{5o}\sin(\theta_o + \delta_{5o})] \tag{19}$$

$$\frac{\delta \mathbf{M} \cdot \hat{\mathbf{b}}_2}{\delta \tilde{u}} = \Big\{ [x_1 \sin(\delta_{1o}) + z_1 \cos(\delta_{1o})] \dots [x_5 \sin(\delta_{5o}) + z_5 \cos(\delta_{5o})] \\ T_{1o}[x_1 \cos(\delta_{1o}) - z_1 \sin(\delta_{1o})] \dots [T_{5o} x_5 \cos(\delta_{5o}) - z_5 \sin(\delta_{5o})] \Big\} \quad (20)$$

Given $\Delta\mathbf{M}$ and $\Delta\mathbf{F}$, weighted least squares (WLS)[21] provides a straightfoward and practical solution to the control allocation problem. The goal is to minimize the errors between the commanded versus delivered incremental forces and moments while minimizing control effector usage about u_o. Equation (21) illustrates the formulation of the WLS cost function:

$$H = \frac{1}{2}\tilde{u}^T R \tilde{u} + \lambda^T (\nu_{\text{cmd}} - B\tilde{u}) \quad (21)$$

where $\nu_{\text{cmd}} = [\Delta\mathbf{M}\ \Delta\mathbf{F}]^T$, B is the control effectiveness matrix and R is a symmetric, positive-definite matrix of size $n \times n$. n presents the number of control inputs. λ is a vector of Lagrange multipliers. The Moore-Penrose generalized solution[21] to the WLS control allocation problem is shown in Eq. (22).

$$\tilde{u} = W^{-1} B^T (B W^{-1} B^T)^{-1} \nu_{\text{cmd}} \quad (22)$$

Elements of the weighting matrix, $W = R^{-1}$, on the thrust and gimbal are shown in Eqs. (23) and (24)

$$W_T^i = \frac{\max(T)}{||B_i||} \quad (23)$$

$$W_\delta^i = \frac{\max(\delta)}{||B_i||} \quad (24)$$

where $\max(T)$ and $\max(\delta)$ are the overall maximum thrust and gimbal limits on the i^{th} rotor. $||B_i||$ represents the norm of the B matrix column associate with the thrust or gimbal of the i^{th} rotor. Procedures for obtaining the control allocation solution is summarized in the following steps:

a) Given θ, $\mathbf{M}_{\text{req}}$, and $\mathbf{F}_{\text{req}}$, look up u_o in the trim map and determine $\mathbf{M}_o$ and $\mathbf{F}_o$

b) Determine $\Delta\mathbf{M}$ and $\Delta\mathbf{F}$

c) Obtain B_{local} in real-time via Eqs. (18) to (20)

d) Determine $\tilde{u}$ using the WLS control allocator

e) Determine the total surface commands, $u_{tot} = u_o + \tilde{u}$

IV. Simulation Results

Figure 9 shows a notional lunar lander training profile. The vehicle initially takes off, climbs, and transitions to horizontal flight using the production control law. Once the desired conditions are met (altitude, heading, velocity, etc.), the vehicle switches over to lunar simulation mode. During lunar simulation mode, the IFT attempts to replicate the HLS closed-loop dynamics with the test pilot in control. At this point, the pilot could either be hands off and let the autopilot land the vehicle automatically, or he/she would attempt to land the vehicle under manual control. Depending on the battery storage capacity, the vehicle may be capable of performing multiple training flights per sortie. In this section, simulation results of the IFT following the last 115 s of the Apollo 11 approach and landing trajectory[22] are shown.

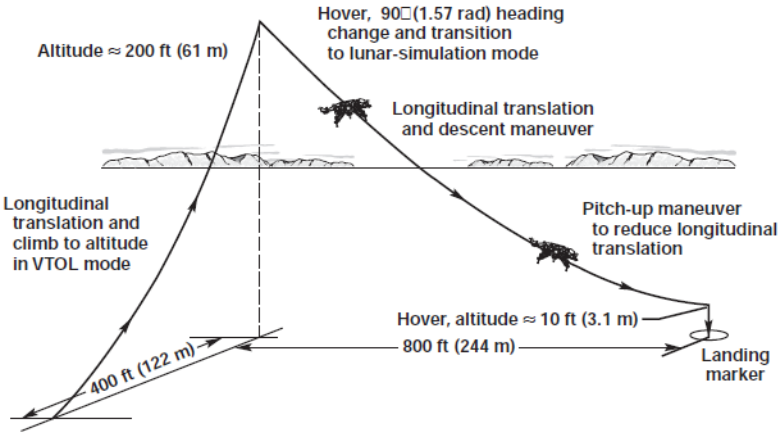

Figure 9. Concept of operation with the IFT, Ref. [2].

In assessing the ability of the vehicle to follow the prescribed trajectory, the reference model block in Fig. 5 is replaced by a set of open-loop commands that consists of the linear and angular velocities/accelerations (V_{ref}, $\dot{V}_{\text{ref}}$, ω_{ref}, $\dot{\omega}_{\text{ref}}$) from Ref. [22]. Time histories of the reference pitch angle, downrange, and altitude profiles are shown in Fig. 10 with touchdown corresponding to time $t = 0$ s. The Apollo 11 reference trajectory is presented by the blue line while the red dashed line indicates the simulated IFT path. The trajectory starts off 827 m uprange and 100 m in altitude from the actual landing site with the vehicle slightly pitched backwards as the Apollo 11 crew switched from P64 (automatic landing mode) to P66 (manual landing mode) a few seconds prior. Subsequently, the crew maneuvered the lander towards the intended landing site by constantly adjusting the pitch attitude via the RHC; hence indirectly, the downrange velocity. At $t = 20$ s, the vehicle is at a near hover over the landing site followed by a constant velocity vertical descent until touchdown.

With the exception of some initial transients due to actuator dynamics, the simulated IFT path closely follows the Apollo 11 trajectory. Thrust and gimbal command time histories are shown in Fig. 11 and within their operational limits. The estimated aerodynamic forces are shown in Fig. 12. At the beginning of the trajectory, these values are significant due to the large dynamic pressure; therefore, more differential thrust is required to compensate for the large nose-down pitching moment. This is apparent in the thrust time history of rotors 5 as they operate close to the lower thrust bound of 2023 N from $t = 115$ to 80 s. Controllability issues arise if the reference trajectory begins sooner; rapidly increasing dynamic pressure causes the simulated control effectors to saturate and preventing the vehicle from operating in lunar simulation mode.

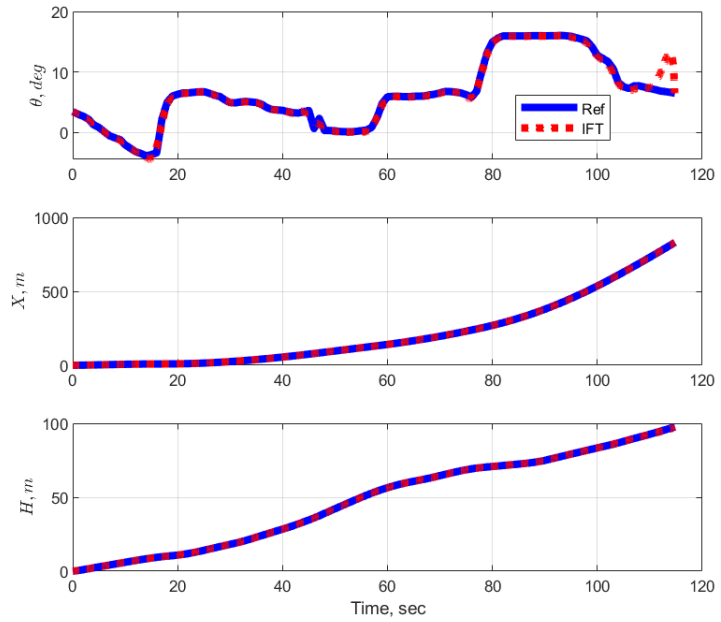

Figure 10. Simulated IFT Path with Reference Apollo 11 Trajectory

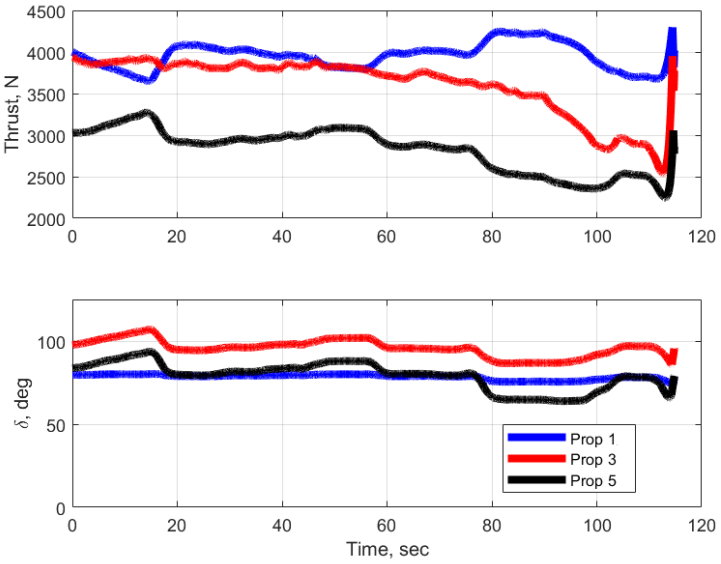

Figure 11. Time Histories of Simulated Rotor Gimbal Angles and Thrusts

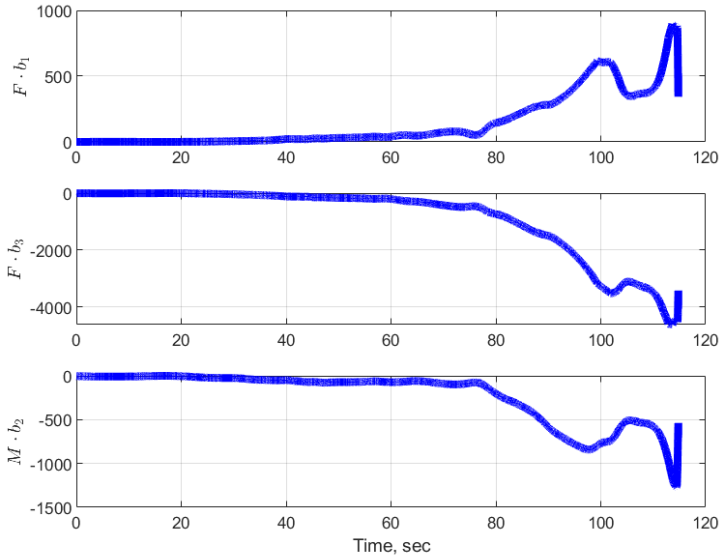

Figure 12. Time Histories of Simulated Aerodynamic Forces and Moment

All six Apollo approach and landing trajectories were similar in nature with relatively shallow flight path angles and low speeds. The gentleness of the trajectories allows the proposed IFT concept to simulate them to a greater extent. For the upcoming Artemis III mission with Lunar Starship,[25] the final approach and landing trajectory will likely be closer to that of Falcon 9 landings[26] with more aggressive maneuvers, rapid descent rates, and flight path angles. The resulting large aerodynamic forces and moments, vortex ring state[27] phenomenon, complex rotor aerodynamic interference effects at high angle-of-attacks, and limited rate capability of the gimbal actuators will severely restrict the duration of the trajectory at which the multi-rotor IFT concept is able to replicate. A well thought out and custom design IFT is likely necessary to encompass the vast differences in vehicle dynamics and approach trajectories of Lunar Starship and future Lunar lander concepts.

V. Summary

This paper explored the viability of leveraging current technology in the field of electric vertical takeoff and landing vehicles as a possible candidate for a lunar landing In-Flight Trainer. The gimbal capability on the multi-tilt-rotor platform enables the vehicle attitude to be decoupled from its flight path, which is a crucial requirement in realistically simulating lunar gravity on Earth. The model-following flight control architecture presented enables the IFT to simulate different lander concepts subjected to its own physical capabilities. Simulation results of the multi-tilt-rotor configuration closely following the final portion of the Apollo 11 descent trajectory are shown.

VI. Acknowledgements

Authors would like to thank Dr. Jeb Orr and Mr. Michael Acheson on their recommendations in the development of the control allocation methodology, Dr. Steven Synder, Mr. Eric Queens, Mr. William Elke, and Mr. Edward Robertson for conducting technical reviews of this work.

References

[1]Gelzer, C., "The Lunar Landing Research Vehicle," *Proceedings of the AIAA SPACE Conference 2006*, AIAA 2006-7468.

[2]Matranga, J. G., Ottinger, C. W., Jarvis, R. C., and Gelzer, D. C., "Unconventional, Contrary, and Ugly," *Monographs in Aerospace History*, NASA SP 2004-4534, Washington, D.C. 2004.

[3]Bellman, R. D., and Matranga, J. G., *Design and Operational Characteristics of a Lunar-Landing Research Vehicle*,

NASA TN D-3023, Edwards, CA, 1965.

[4]Jarvis, R. C., *Operational Experience with the Electronic Flight Control Systems of a Lunar-Landing Research Vehicle*, NASA TN D-3689, Edwards, CA, 1966.

[5]Kluever, E. E., Mallick, L. D., and Matranga, J. G., "Flight Results with a Non-Aerodynamic, Variable Stability, Flying Platform," *Society of Experimental Test Pilots*, Vol. 8, No. 2, 1966.

[6]Jarvis, R. C., "Fly-by-wire Flight Control System Experience with a Free-Flight Lunar-Landing Research Vehicle," *Proceedings of the AIAA Flight Test, Simulation, and Support Conference 1967*, AIAA 67-273.

[7]Armstrong, A. N., "Flight Testing the Lunar Landing Research and Lunar Landing Training Vehicles," *Society of Experimental Test Pilots*, 2009.

[8]"NASA's Lunar Exploration Program Overview," September, 2020. `https://www.nasa.gov/sites/default/files/atoms/files/artemis_plan-20200921.pdf` [accessed 26 December, 2020].

[9]Lombaerts, T., Laneshige, J., Schuet, S., Hardy, G., Aponso, B., and Shish, K., "Dynamic Inversion based Full Envelope Flight Control for an eVTOL Vehicle using a Unified Framework," AIAA-1619.

[10]"NASA Begins Air Taxi Flight Testing with Joby," September, 2021. `https://www.nasa.gov/press-release/nasa-begins-air-taxi-flight-testing-with-joby` [accessed 19 May, 2022].

[11]Duda, R. K., Johnson, C. M., and Fill, J. T., "Design and Analysis of Lunar Lander Manual Control Modes," IEEEAC 2009-1180.

[12]Klumpp, R. A., "A Manually Retargeted Automatic Landing System for the Lunar Module", *Journal of Spacecraft and Rockets*, Vol. 5, No. 2, 1968.

[13]Miller, C., "Nonlinear Dynamic Inversion Baseline Control Law: Architecture and Performance Predictions," AIAA 2011-6467.

[14]Stevens, L. B., and Lewis, L. F., *Aircraft Control and Simulation*, John Wiley & Sons, Inc, Hoboken, NJ. 2003.

[15]Harris, J., and Stanford, J., "F-35 Flight Control Law Design, Development, and Verification," *Proceedings of the AIAA Aviation Forum 2018*, AIAA 2018-3516.

[16]Canin, G. D., McConnell, K. J., and James, W. P., "F-35 High Angle of Attack Flight Control Development and Flight Test Results," *Proceedings of the AIAA Aviation Forum 2019*, AIAA 2019-3227.

[17]"OpenVSP wiki," May, 2020. `https://http://http://openvsp.org/wiki/doku.php?id=start` [accessed 26 December, 2020].

[18]"Lunar Landing Training Vehicle Trade Study Interim Report to the Lunar Lander Project Office, Volumes I and II," Edwards, CA, 2008.

[19]Mathworks. *Optimization Toolbox*, 2016.

[20]McVeigh, M., Grauer, W., Paisley, D., "Rotor/Airframe Interactions on Tiltrotor Aircraft", *Journal of the American Helicopter Society*, July 1990.

[21]Durham, W., Bordignon, A. K., and Beck, R., *Aircraft Control Allocation*, John Wiley & Sons, Ltd, UK. 2017.

[22]Bennett, F., "Apollo Lunar Descent and Ascent Trajectories," NASA TM X-58040, March 1970.

[23]"Flying the V-22," March, 2012. `https://verticalmag.com/features/20112-flying-the-v-22-html/` [accessed 26 December, 2020].

[24]Rosenstein, H., and Clark, R., "Aerodynamic Development of the V-22 Tilt Rotor," AIAA 86-2678.

[25]`https://www.https://www.nasa.gov/press-release/as-artemis-moves-forward-nasa-picks-spacex-to-land-next-americans-on-moon` [accessed 11, November, 2022].

[26]`https://en.wikipedia.org/wiki/Falcon_9_first-stage_landing_tests` [accessed 11, November, 2022].

[27]Prouty, W. R., *Helicopter Aerodynamics*, Helobooks. 2004.